

A theoretically exact reconstruction algorithm for helical cone-beam differential phase-contrast computed tomography

This content has been downloaded from IOPscience. Please scroll down to see the full text.

2013 Phys. Med. Biol. 58 5421

(<http://iopscience.iop.org/0031-9155/58/16/5421>)

View [the table of contents for this issue](#), or go to the [journal homepage](#) for more

Download details:

IP Address: 129.129.158.103

This content was downloaded on 06/01/2014 at 08:49

Please note that [terms and conditions apply](#).

A theoretically exact reconstruction algorithm for helical cone-beam differential phase-contrast computed tomography

Jing Li¹, Yi Sun^{1,3} and Peiping Zhu²

¹ School of Information and Communication Engineering, Dalian University of Technology, Dalian, Liaoning Province 116023, People's Republic of China

² Institute of High Energy Physics, Chinese Academy of Sciences, Beijing 100049, People's Republic of China

E-mail: dlutburnsky@aliyun.com (J Li), ls1wf@dlut.edu.cn (Y Sun) and zhupp@ihep.ac.cn (P Zhu)

Received 15 May 2013, in final form 11 June 2013

Published 23 July 2013

Online at stacks.iop.org/PMB/58/5421

Abstract

Differential phase-contrast computed tomography (DPC-CT) reconstruction problems are usually solved by using parallel-, fan- or cone-beam algorithms. For rod-shaped objects, the x-ray beams cannot recover all the slices of the sample at the same time. Thus, if a rod-shaped sample is required to be reconstructed by the above algorithms, one should alternately perform translation and rotation on this sample, which leads to lower efficiency. The helical cone-beam CT may significantly improve scanning efficiency for rod-shaped objects over other algorithms. In this paper, we propose a theoretically exact filter-backprojection algorithm for helical cone-beam DPC-CT, which can be applied to reconstruct the refractive index decrement distribution of the samples directly from two-dimensional differential phase-contrast images. Numerical simulations are conducted to verify the proposed algorithm. Our work provides a potential solution for inspecting the rod-shaped samples using DPC-CT, which may be applicable with the evolution of DPC-CT equipments.

(Some figures may appear in colour only in the online journal)

1. Introduction

X-ray differential phase-contrast CT (DPC-CT) reveals a sample's internal structure by using x-ray refraction information rather than the attenuation (Nilchian *et al* 2013, Xu *et al* 2012), which is considered a promising medical diagnosis and/or non-destructive technique, and a possible alternative to conventional x-ray CT for providing higher contrast between soft tissues (Bravin *et al* 2013, Suetens 2009, Vedantham and Karellas 2013). Currently, the

³ Author to whom any correspondence should be addressed.

refraction information, the gradient of the x-ray transform of the sample's refractive-index distribution, can be retrieved by an analyzer-based-imaging (ABI) (Diemoz *et al* 2010) or a grating-based method. The ABI method mainly relies on the high coherence of synchrotron-radiation sources, which is the main obstacle in the realization of the practical DPC-CT system. Grating-based imaging, including interferometric (Zanette *et al* 2011, Pfeiffer *et al* 2006) and/or noninterferometric (Olivo *et al* 2011, Huang *et al* 2009, Munro *et al* 2010, 2012) methods, seems more promising than ABI in realizing the compact DPC-CT system, since these methods allow the use of a laboratory x-ray tube. One-dimensional (1D) gratings have been widely used in current DPC-imaging and DPC-CT experiments. However, the 1D gratings can only capture the component of the refraction angle of x-rays in the direction perpendicular to the grating lines. Kottler *et al* (2007) showed that two-dimensional (2D) phase-contrast images can be achieved by the use of 1D gratings with rotation. In order to overcome this limitation, several DPC-imaging methods using 2D gratings were proposed (Wen *et al* 2010, Itoh *et al* 2011, Sato *et al* 2011), which may provide multi-direction refraction information without grating-rotation.

In synchrotron-radiation-based DPC-CT experiments, the radiation source is usually placed far enough away from the sample and the beams can be well approximated as parallel beams. In this case, the DPC-CT reconstruction problem can be solved by parallel-beam algorithms (Chong *et al* 2012, Zhu *et al* 2010, Lauzier *et al* 2012). In grating-based DPC-CT experiments, the laboratory x-ray tube or microfocus source emits spherical waves, where the fan-beam (Wu *et al* 2013, Fu *et al* 2011, Chen and Qi 2008) or the cone-beam (Fu *et al* 2012, Bevins *et al* 2012) algorithms are more suitable than parallel-beam algorithms. For rod-shaped samples, due to the limitation of the grating size, the fan or cone beams cannot recover the whole object at the same time. Thus, if a rod-shaped sample is required to be reconstructed by the above algorithms, one should alternately perform translation and rotation on this sample. Helical cone-beam CT allows the translation and rotation operations to be performed simultaneously, which may be more efficient than other algorithms in the case of rod-shaped samples.

In absorption-based helical cone-beam CT, the reconstruction problem can be theoretically exactly solved by Tuy's formula (Tuy 1983), Katsevich's algorithm (Katsevich 2002, 2004, Tan *et al* 2012, Noo *et al* 2003, Yu and Wang 2004) or Zou–Pan's algorithm (Zou *et al* 2004). In some sense, Tuy's formula can be seen as a fundamental theory accommodating Katsevich's algorithm and Zou–Pan's algorithm; Zou–Pan's algorithm can be treated as a backprojected-filtration structure of Katsevich's algorithm. In 2011, the feasibility of the combination of the helical scanner and the Talbot–Lau interferometer was initially demonstrated by Qi *et al* (2011). Like that for conventional helical cone-beam CT, the reconstruction problem for helical DPC-CT was also first solved by an interpolation-based algorithm, which approximates the cone-beam geometry by multiple parallel fan beams and estimates the sinogram of a given slice from neighboring fan beams using linear interpolation. The given slices can be reconstructed by fan-beam algorithms from the synthesized sinograms. Thus, the image artifacts are usually caused by the estimation errors of the sinograms. In 2012, our group reported another approximate algorithm (Li *et al* 2012), where the helical arc specified by a PI-line segment is approximated as a circular arc located at a slant plane, such that the PI-line-based fan-beam DPC-CT algorithm can be implemented. Although this algorithm achieves satisfactory reconstructions in many cases, it still suffers the problem of theoretical support. For example, if the sample deviates the x-ray beam at large angles along the vertical direction, this algorithm will provide low-quality reconstructions, which will be demonstrated in section 3.2.

Thus, we propose a theoretically exact algorithm to provide higher quality results for helical DPC-CT. In this paper, we derive a data conversion scheme, according to which

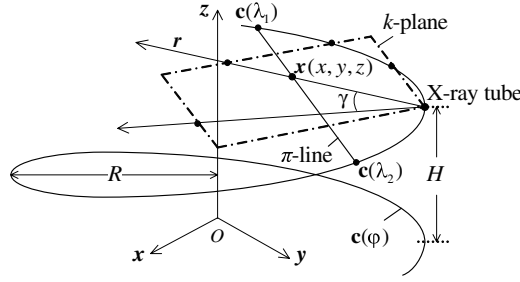


Figure 1. Geometry of a helical cone-beam CT. The x-ray tube moves along the helical curve $c(\varphi) = (R \cos \varphi, R \sin \varphi, H\varphi/2\pi)$, with the radii R and pitch H . The π -line intersects the x-ray source trajectory at two points, $c(\lambda_1)$ and $c(\lambda_2)$, whose angular parameters are λ_1 and λ_2 , respectively. The k -plane is any plane that contains the point \mathbf{x} and has three intersections with the helical curve such that one intersection is at the intermediate position of the helical arc specified by the other two points.

the theoretically exact filter-backprojection (FBP) algorithm is developed by modifying the Katsevich algorithm. This algorithm can be applied to reconstruct the refractive index decrement of the samples directly from the 2D refraction-angle data. However, if 1D gratings were employed, the acquisition of 2D refraction-angle data requires grating-rotation. Thus, we also provide an approximate implementation of the proposed algorithm by neglecting the vertical component of the 2D refraction-angle data, which does not require the grating-rotation. Our paper may be valuable for those who are interested in the Katsevich algorithm and DPC-CT.

We organize the paper as follows. In section 2, we introduce the mathematical theory of our algorithm. In section 3, we show the numerical simulations of the proposed algorithms. Finally, a conclusion is given in section 4.

2. Methods

In this section, Katsevich's formula is firstly described. After that, we will derive our theoretically exact FBP algorithm for helical cone-beam DPC-CT by modifying Katsevich's algorithm. Throughout this paper, the refractive index decrement of the 3D object to be reconstructed is denoted as a function $\delta(x, y, z)$ which is zero outside the cylinder containing the helical locus.

2.1. Katsevich algorithm

The geometry of the helical cone-beam CT scanner is shown in figure 1. Obviously, each x-ray beam can be specified by the ray's direction \mathbf{r} and the rotation angle φ . Katsevich's formula is based on the concept of the π -line. As shown in figure 1, for each point \mathbf{x} , there is one and only one π -line passing through this point and connecting two points of the helical x-ray trajectory at each turn (Katsevich 2002, 2004, Yu and Wang 2004).

According to Katsevich's theory, the value of the refractive index decrement δ of the point \mathbf{x} can be reconstructed by the following equation (Katsevich 2004):

$$\delta(x, y, z) = \frac{-1}{2\pi^2} \int_{\lambda_2}^{\lambda_1} d\varphi \frac{1}{|\mathbf{x} - \mathbf{c}(\varphi)|} \int_0^{2\pi} \frac{\partial \Theta(\varphi, \mathbf{r})}{\partial \varphi} \frac{d\gamma}{\sin \gamma}, \quad (1)$$

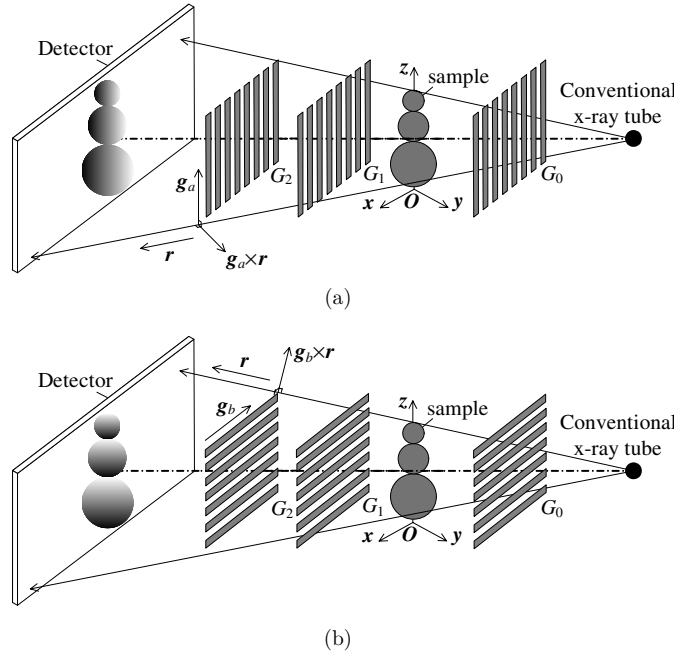


Figure 2. Cone-beam DPC imaging using one-dimensional gratings. (a) The DPC-imaging system with vertical grating lines. (b) The DPC-imaging system with horizontal grating lines. The imaging systems consist of three gratings: G_0 , G_1 and G_2 . The sample can be placed before or behind the grating G_1 . The flat detector should be placed immediately behind the grating G_2 .

where $c(\varphi)$ denotes the position of the x-ray tube, λ_1 and λ_2 are the angular parameters of the two end points of the π -line and γ denotes the angle between the x-ray passing through the point x and other rays belonging to the k -plane, as shown by figure 1. $\Theta(\varphi, \mathbf{r})$ is the x-ray transform of the refractive index decrement δ along the x-ray path:

$$\Theta(\varphi, \mathbf{r}) = \int_{-\infty}^{+\infty} \delta(\mathbf{c}(\varphi) + t\mathbf{r}) dt. \quad (2)$$

If $\Theta(\varphi, \mathbf{r})$ is obtained, then equation (1) can be directly implemented. However, the DPC-CT equipments provide the refraction-angle data θ , not the x-ray transform $\Theta(\varphi, \mathbf{r})$. Thus, equation (1) cannot be implemented for helical cone-beam DPC-CT unless some changes are made.

2.2. Formulae for helical cone-beam DPC-CT

Several groups have realized the cone-beam differential phase-contrast imaging by the use of 1D gratings. Their implementations have a similar geometry, as shown in figures 2(a) and (b). In interferometric methods (Zanette *et al* 2011, Pfeiffer *et al* 2006), the openings of the source grating G_0 should be narrow enough to provide spatially coherent x-rays. In noninterferometric methods (Olivo *et al* 2011, Huang *et al* 2009, Munro *et al* 2010, 2012), the source grating G_0 is used to improve the visibility of the projections (Huang *et al* 2009), and can be neglected if the focal spot is small enough, e.g. $\leq 100 \mu\text{m}$ (Olivo *et al* 2011, Munro *et al* 2012). In the two types of grating-based-imaging methods mentioned above, the grating G_1 is used as a splitter to produce periodic fringes through the Talbot self-imaging or geometric projection; the grating

G_2 with the same period as the periodic fringes works as a gate to allow or prohibit most of the rays to be collected by the detector. If a sample is placed either before or after the grating G_1 , the refraction changes the location of the fringes and further changes the intensity on the detector. The measured projection data are essentially the refraction angles of the incident beams.

In general, the 1D gratings can only detect refractive deviation of x-rays in the direction perpendicular to the grating lines. If the gratings with vertical lines are employed, the measured projection data are essentially the horizontal component $\theta_a(\varphi, \mathbf{r})$ of the refraction angle, as shown in figure 2(a). According to Snell's law, the relationship between the measured refraction-angle data $\theta_a(\varphi, \mathbf{r})$ and the direction \mathbf{g}_a of the gratings can be described as

$$\theta_a(\varphi, \mathbf{r}) = \int \left\langle \nabla \delta(\mathbf{c}(\varphi) + t\mathbf{r}), \frac{\mathbf{r} \times \mathbf{g}_a}{|\mathbf{r} \times \mathbf{g}_a|} \right\rangle dt, \quad (3)$$

where $\nabla \delta$ denotes the gradient vector of the function $\delta(x, y, z)$, \mathbf{r} represents the direction vector of the x-ray, \times means the cross product and $\langle \cdot \rangle$ means the inner product. Similarly, the vertical component $\theta_b(\varphi, \mathbf{r})$ of the refraction angle can be obtained by rotating the gratings by 90° , as shown in figure 2(b). The measured refraction-angle data $\theta_b(\varphi, \mathbf{r})$ can be expressed as

$$\theta_b(\varphi, \mathbf{r}) = \int \left\langle \nabla \delta(\mathbf{c}(\varphi) + t\mathbf{r}), \frac{\mathbf{r} \times \mathbf{g}_b}{|\mathbf{r} \times \mathbf{g}_b|} \right\rangle dt, \quad (4)$$

where \mathbf{g}_b denotes the direction of the grating lines shown in figure 2(b).

Now, we focus on the derivative data $\partial \Theta(\varphi, \mathbf{r}) / \partial \varphi$ employed in equation (1), that is,

$$\frac{\partial \Theta(\varphi, \mathbf{r})}{\partial \varphi} = \lim_{\varepsilon \rightarrow 0} \frac{\Theta(\varphi + \varepsilon, \mathbf{r}) - \Theta(\varphi, \mathbf{r})}{\varepsilon}. \quad (5)$$

By modifying equation (5) using equation (2), one can easily work out the following equation by using the Taylor series expansion:

$$\begin{aligned} \frac{\partial \Theta(\varphi, \mathbf{r})}{\partial \varphi} &= \lim_{\varepsilon \rightarrow 0} \frac{\int_{-\infty}^{+\infty} [\delta(\mathbf{c}(\varphi + \varepsilon) + t\mathbf{r}) - \delta(\mathbf{c}(\varphi) + t\mathbf{r})] dt}{\varepsilon} \\ &= \lim_{\varepsilon \rightarrow 0} \frac{\int_{-\infty}^{+\infty} \langle \nabla \delta(\mathbf{c}(\varphi) + t\mathbf{r}), \mathbf{c}'(\varphi) \varepsilon \rangle dt}{\varepsilon} \\ &= \int_{-\infty}^{+\infty} \langle \nabla \delta(\mathbf{c}(\varphi) + t\mathbf{r}), \mathbf{c}'(\varphi) \rangle dt, \end{aligned} \quad (6)$$

where $\mathbf{c}'(\varphi) = R(-\sin \varphi, \cos \varphi, H/2\pi R)$ denotes the tangential vector of the helical locus, which can always be expressed as the linear combination of the three vectors \mathbf{r} , $\frac{\mathbf{r} \times \mathbf{g}_a}{|\mathbf{r} \times \mathbf{g}_a|}$ and $\frac{\mathbf{r} \times \mathbf{g}_b}{|\mathbf{r} \times \mathbf{g}_b|}$, that is,

$$\mathbf{c}'(\varphi) = \sigma \mathbf{r} + \zeta \frac{\mathbf{r} \times \mathbf{g}_a}{|\mathbf{r} \times \mathbf{g}_a|} + \tau \frac{\mathbf{r} \times \mathbf{g}_b}{|\mathbf{r} \times \mathbf{g}_b|}, \quad (7)$$

where σ , ζ and τ are coefficients. Substituting equation (7) into equation (6), we have the following equation:

$$\frac{\partial \Theta(\varphi, \mathbf{r})}{\partial \varphi} = \int \left\langle \nabla \delta(\mathbf{c}(\varphi) + t\mathbf{r}), \sigma \mathbf{r} + \zeta \frac{\mathbf{r} \times \mathbf{g}_a}{|\mathbf{r} \times \mathbf{g}_a|} + \tau \frac{\mathbf{r} \times \mathbf{g}_b}{|\mathbf{r} \times \mathbf{g}_b|} \right\rangle dt. \quad (8)$$

Note that the inner product $\langle \nabla \delta(\mathbf{c}(\varphi) + t\mathbf{r}), \mathbf{r} \rangle$ means the gradient of the object function δ along the x-ray path. Thus, we have

$$\int \langle \nabla \delta(\mathbf{c}(\varphi) + t\mathbf{r}), \mathbf{r} \rangle dt \equiv 0. \quad (9)$$

Substituting equations (3), (4) and (9) into equation (8), we work out the relationship between derivative data $\partial\Theta(\varphi, \mathbf{r})\partial\varphi$ and the refraction-angle data $\theta_a(\varphi, \mathbf{r})$ and $\theta_b(\varphi, \mathbf{r})$, that is,

$$\frac{\partial\Theta(\varphi, \mathbf{r})}{\partial\varphi} = \zeta\theta_a(\varphi, \mathbf{r}) + \tau\theta_b(\varphi, \mathbf{r}). \quad (10)$$

The general formulation of the proposed algorithm can be easily obtained by substituting equation (10) into equation (1):

$$\delta(x, y, z) = \frac{-1}{2\pi^2} \int_{\lambda_2}^{\lambda_1} d\varphi \frac{1}{|\mathbf{x} - \mathbf{c}(\varphi)|} \int_0^{2\pi} [\zeta\theta_a(\varphi, \mathbf{r}) + \tau\theta_b(\varphi, \mathbf{r})] \frac{d\gamma}{\sin \gamma}. \quad (11)$$

Recently, some papers have recommended curved gratings (Revol *et al* 2010) instead of flat gratings, since the curved gratings may enlarge the fields of view. Equation (11) would also be applicable if the curved gratings introduced in Revol *et al* (2010) were employed, since the vector directions \mathbf{g}_a and \mathbf{g}_b of the grating lines remain the same. Note that the two vectors $\frac{\mathbf{r} \times \mathbf{g}_a}{|\mathbf{r} \times \mathbf{g}_a|}$ and $\frac{\mathbf{r} \times \mathbf{g}_b}{|\mathbf{r} \times \mathbf{g}_b|}$ are perpendicular to the vector \mathbf{r} . We have

$$\begin{aligned} \left\langle \frac{\mathbf{r} \times \mathbf{g}_a}{|\mathbf{r} \times \mathbf{g}_a|}, \mathbf{r} \right\rangle &\equiv 0 \\ \left\langle \frac{\mathbf{r} \times \mathbf{g}_b}{|\mathbf{r} \times \mathbf{g}_b|}, \mathbf{r} \right\rangle &\equiv 0. \end{aligned} \quad (12)$$

Using the above two equations, one can derive the two equations shown in equation (13) from equation (7):

$$\begin{aligned} \left\langle \mathbf{c}'(\varphi), \frac{\mathbf{r} \times \mathbf{g}_a}{|\mathbf{r} \times \mathbf{g}_a|} \right\rangle &= \zeta + \left\langle \frac{\mathbf{r} \times \mathbf{g}_a}{|\mathbf{r} \times \mathbf{g}_a|}, \frac{\mathbf{r} \times \mathbf{g}_b}{|\mathbf{r} \times \mathbf{g}_b|} \right\rangle \tau \\ \left\langle \mathbf{c}'(\varphi), \frac{\mathbf{r} \times \mathbf{g}_b}{|\mathbf{r} \times \mathbf{g}_b|} \right\rangle &= \tau + \left\langle \frac{\mathbf{r} \times \mathbf{g}_a}{|\mathbf{r} \times \mathbf{g}_a|}, \frac{\mathbf{r} \times \mathbf{g}_b}{|\mathbf{r} \times \mathbf{g}_b|} \right\rangle \zeta. \end{aligned} \quad (13)$$

According to the two relationships shown in equation (13), one can easily obtain the two coefficients ζ and τ employed in equation (11). They are

$$\begin{aligned} \zeta &= \frac{\left\langle \mathbf{c}'(\varphi), \frac{\mathbf{r} \times \mathbf{g}_a}{|\mathbf{r} \times \mathbf{g}_a|} \right\rangle - \left\langle \mathbf{c}'(\varphi), \frac{\mathbf{r} \times \mathbf{g}_b}{|\mathbf{r} \times \mathbf{g}_b|} \right\rangle \cdot \left\langle \frac{\mathbf{r} \times \mathbf{g}_a}{|\mathbf{r} \times \mathbf{g}_a|}, \frac{\mathbf{r} \times \mathbf{g}_b}{|\mathbf{r} \times \mathbf{g}_b|} \right\rangle}{1 - \left\langle \frac{\mathbf{r} \times \mathbf{g}_a}{|\mathbf{r} \times \mathbf{g}_a|}, \frac{\mathbf{r} \times \mathbf{g}_b}{|\mathbf{r} \times \mathbf{g}_b|} \right\rangle^2} \\ \tau &= \frac{\left\langle \mathbf{c}'(\varphi), \frac{\mathbf{r} \times \mathbf{g}_b}{|\mathbf{r} \times \mathbf{g}_b|} \right\rangle - \left\langle \mathbf{c}'(\varphi), \frac{\mathbf{r} \times \mathbf{g}_a}{|\mathbf{r} \times \mathbf{g}_a|} \right\rangle \cdot \left\langle \frac{\mathbf{r} \times \mathbf{g}_a}{|\mathbf{r} \times \mathbf{g}_a|}, \frac{\mathbf{r} \times \mathbf{g}_b}{|\mathbf{r} \times \mathbf{g}_b|} \right\rangle}{1 - \left\langle \frac{\mathbf{r} \times \mathbf{g}_a}{|\mathbf{r} \times \mathbf{g}_a|}, \frac{\mathbf{r} \times \mathbf{g}_b}{|\mathbf{r} \times \mathbf{g}_b|} \right\rangle^2}. \end{aligned} \quad (14)$$

Equation (11) requires that the sample be reconstructed from the 2D refraction-angle data. However, if 1D gratings were employed, the acquisition of 2D refraction-angle data requires grating-rotation. If one of the two components, either $\zeta\theta_a(\varphi, \mathbf{r})$ or $\tau\theta_b(\varphi, \mathbf{r})$, produces fewer contribution for reconstructions, the grating-rotation can be avoided by neglecting this component. It will not be hard to prove that the coefficient τ/ζ tends to zero if the radii of the helical locus $\mathbf{c}(\varphi)$ tends to infinity, which leads to our approximate formula by neglecting the vertical component $\theta_b(\varphi, \mathbf{r})$. This formula can be written as

$$\delta(x, y, z) = \frac{-1}{2\pi^2} \int_{\lambda_2}^{\lambda_1} d\varphi \frac{1}{|\mathbf{x} - \mathbf{c}(\varphi)|} \int_0^{2\pi} \zeta\theta_a(\varphi, \mathbf{r}) \frac{d\gamma}{\sin \gamma}. \quad (15)$$

Of course, if the vertical component $\theta_b(\varphi, \mathbf{r})$ of the refraction angle is much larger than the horizontal component $\theta_a(\varphi, \mathbf{r})$, equation (15) may provide low-quality reconstructions for neglecting the component $\tau\theta_b(\varphi, \mathbf{r})$.

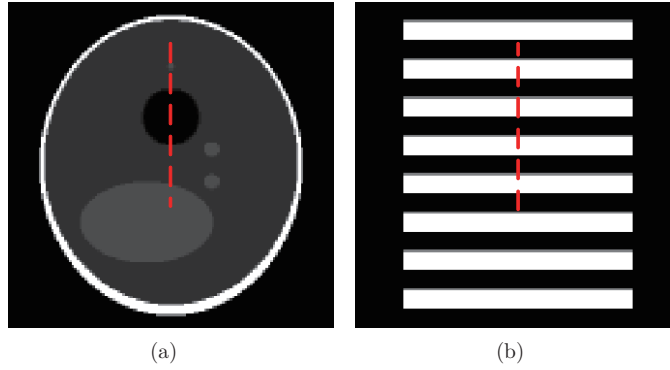


Figure 3. Typical slices of the Shepp–Logan phantom and our disc phantom. (a) Vertical slice of the Shepp–Logan phantom at $y = 0$. (b) Vertical slice of the disc phantom at $y = 0$. The (red) dashed lines in (a) and (b) are used for the intensity profile.

If the Fourier-based phase-retrieval method (Bevins *et al* 2012) which does not require phase-stepping could be employed in helical DPC-CT, the data-acquisition and reconstruction schemes for helical DPC-CT can be performed like those for conventional helical CT, by using equation (15). The implementations of our algorithms are similar to that of Katsevich's algorithm (Noo *et al* 2003, Yu and Wang 2004).

3. Simulations

To verify the performance of the methods illustrated above, we make two sets of numerical studies. All numerical experiments were conducted on our workstation with an Intel Pentium Dual E2160 CPU and 2GB RAM. MATLAB 7.0.1 was chosen to implement the algorithms. The 3D Shepp–Logan phantom shown by figure 3(a) and our disc phantom shown by figure 3(b) were adopted to demonstrate the proposed algorithms. Our disc phantom contains eight short cylinders, and the diameter and height of each cylinder are 79.3 mm and 5.8 mm, respectively. The values of the two phantoms were linearly mapped to 0 – 10^{-6} to represent the distribution of the refractive index decrement $\delta(x, y, z)$. The parameters of the geometrical configurations of the two numerical experiments are displayed in table 1.

3.1. Simulations using the Shepp–Logan phantom

In this section, we evaluated the efficiency and stability of the proposed algorithms. The parameters of the geometrical configuration of this experiment are displayed in table 1. The two components of the refraction-angle data, $\theta_a(\varphi, \mathbf{r})$ and $\theta_b(\varphi, \mathbf{r})$, were analytically calculated according to equations (3) and (4) using the 3D Shepp–Logan model. For convenience, we assume that the projections are collected by a flat detector. Two typical refraction-angle projections are displayed in figure 4. We added zero-mean Gaussian noise to the noise-free refraction-angle data sets. The standard deviation of the Gaussian noise is 0.2 times that of the refraction-angle data. We implemented equations (11) and (15) and the slant fan-beam algorithm (Li *et al* 2012) to reconstruct the slices at $y = 0$, respectively. The reconstructed images are shown in figure 5.

Comparing with the disc phantom, the Shepp–Logan model is much smoother along the vertical direction and causes less vertical deviation of x-rays. Thus, the approximate algorithms also achieve satisfactory reconstructions. The intensity profiles of the reconstructions along



Figure 4. Refraction-angle projection of the Shepp–Logan phantom. (a) The horizontal component. (b) The vertical component.

Table 1. Geometrical configuration.

Parameters	Values
Source-to-rotation-axis distance (mm)	600
Axis-to-detector distance (mm)	100
Helical pitch (mm)	100
Sides of phantoms (mm)	100
Resolution of phantoms	$256 \times 256 \times 256$
Scanning step angle	1°
Scanning range	$-3\pi-3\pi$
Number of detectors per row	366
Number of detectors per column	140
Detector length (mm)	166.8
Detector height (mm)	63.8
Reconstruction matrix	$128 \times 128 \times 128$

the central (red) dashed line of figure 3(a) are displayed in figure 5(d). One can clearly see that the reconstructed values match the true values very well, which verify the correctness of our algorithms. To further compare the above reconstruction results, we calculate the peak-signal-to-noise-ratio (PSNR) of the three reconstructed images in figure 5. The PSNR values of the reconstructed images, from figures 5(a) to (c), are 27.84 dB, 27.43 dB and 26.45 dB, respectively. Obviously, in this simulation, the neglecting of the vertical components employed in equation (11) reduces the PSNR of the reconstructed images to about only 0.4 dB.

3.2. Simulations using the disc phantom

In this section, we performed the same simulation using the disc phantom shown by figure 3(b), to illustrate the limitation of approximate algorithms and the superiority of the theoretically exact algorithm. The horizontal and vertical components of refraction-angle data were analytically calculated according to equations (3) and (4). Two typical refraction-angle data are displayed in figure 6.

We implemented the two proposed algorithms and the slant fan-beam algorithm (Li *et al* 2012) to reconstruct the slices at $y = 0$ from noise-free refraction-angle data. The reconstructions are displayed in figures 7(a)–(c). Figure 7(a) is the reconstructed image of equation (11), where the artifacts are invisible. Unlike the Shepp–Logan phantom, the disc phantom contains a lot of cross-sections, which cause serious refractive deviation of x-rays along the vertical direction. Thus, the neglecting of the component $\tau\theta_b(\varphi, \mathbf{r})$ from equation (11) will manifest streak-shaped artifacts around each cross-section, as shown in figure 7(b). Figure 7(c) is the reconstruction of the slant fan-beam algorithm, which also contains significant streak-shaped artifacts.

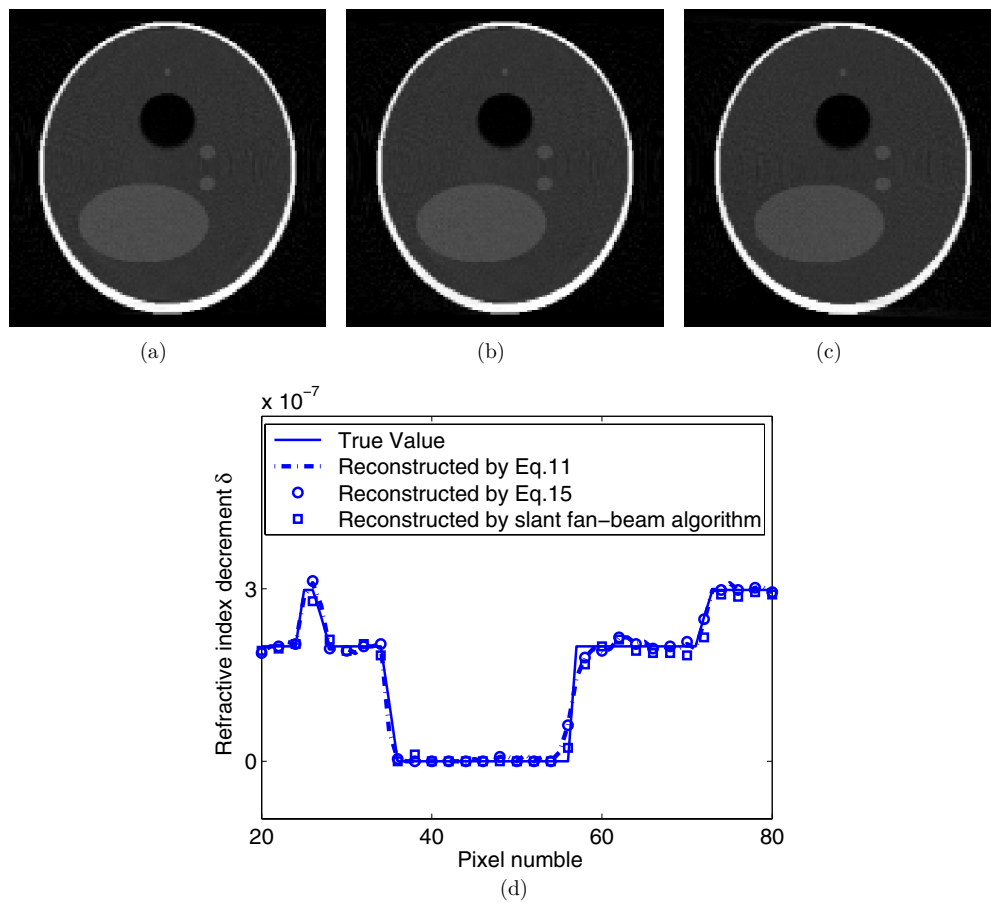


Figure 5. Reconstructed slices of the 3D Shepp-Logan phantom at $y = 0$. (a) The slice reconstructed by equation (11). (b) The slice reconstructed by equation (15). (c) The slice reconstructed by slant fan-beam algorithm. (d) The intensity profiles along the (red) dashed line in figure 3(a). All the reconstructions are linearly mapped to the grayscale range of 0–255, after their negative values are removed.



Figure 6. Refraction-angle projection of the disc phantom. (a) The horizontal component. (b) The vertical component.

To further compare the above reconstruction results, we calculated the intensity profiles along the (red) dashed line in figure 3(b). The intensity profiles are shown in figure 7(d). Obviously, the reconstruction of the theoretically exact algorithm shows better agreement with the theoretical values than that of the two approximate algorithms. The PSNR values

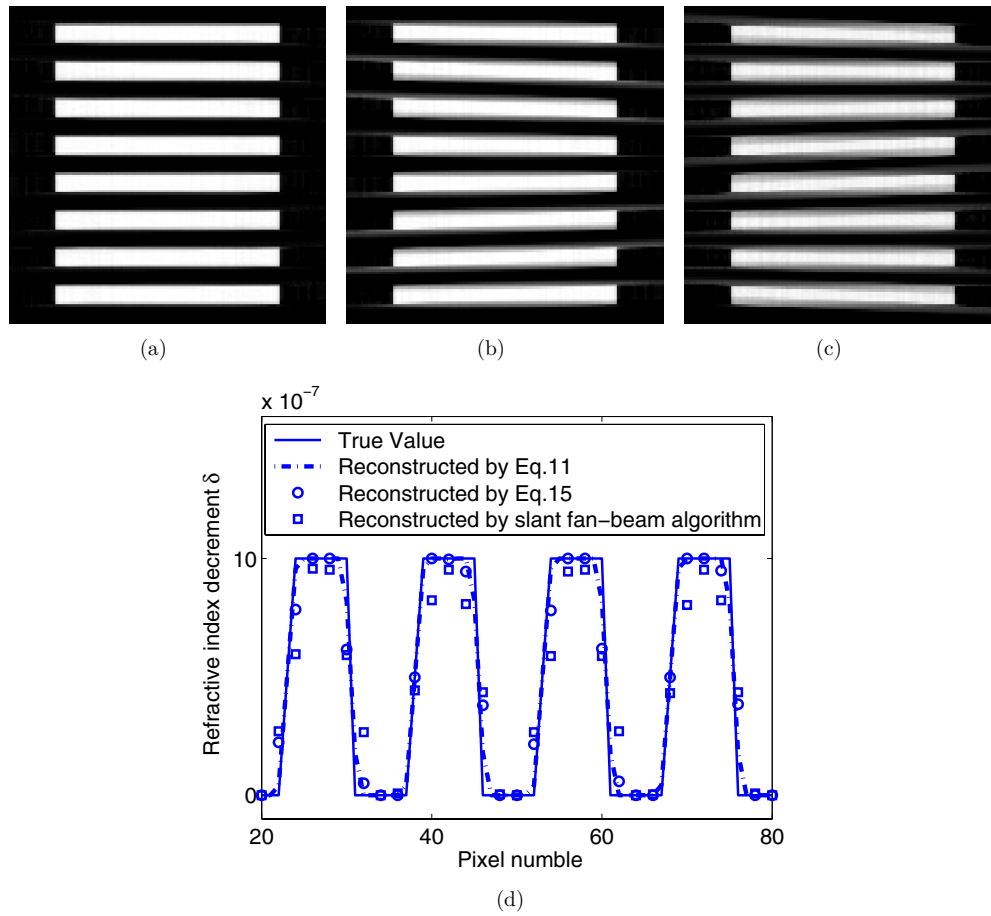


Figure 7. Reconstructed slices of the disc phantom at $y = 0$. (a) The slice reconstructed by equation (11). (b) The slice reconstructed by equation (15). (c) The slice reconstructed by the slant fan-beam algorithm. (d) The intensity profiles along the (red) dashed line in figure 3(b). All the reconstructions are linearly mapped to the grayscale range of 0–255, after their negative values are removed.

of the reconstructed images, from figures 7(a) to (c), are 25.60 dB, 17.44 dB and 15.40 dB, respectively. It should be pointed out that the difference between equation (15) and the slant fan-beam algorithm is the choice of the filtering path. equation (15) filters the refraction-angle data along the k -lines, while the slant fan-beam algorithm filters the refraction-angle data along the π -lines. However, comparing with the neglecting of the component $\tau_{\theta_b}(\varphi, \mathbf{r})$, this difference yields smaller impact on the reconstructions, about only 1–2 dB in our simulation. Thus, for the sample that deviates the x-ray at large angles along the vertical direction, the approximate algorithms are not recommended.

4. Conclusion and future work

This paper establishes a general relationship between the derivative data $\partial\Theta(\varphi, \mathbf{r})/\partial\varphi$ and the x-ray refraction-angle data; thereby, Katsevich's formula can be adopted and modified to obtain a theoretically exact reconstruction for helical cone-beam DPC-CT. With this relationship,

many other algorithms for conventional CT may also be extended to the DPC-CT area, such as Zou–Pan’s algorithm (Zou *et al* 2004) which may be suitable for truncated data. In the future, we will carry out our research on this topic and the variable radius helical cone-beam DPC-CT reconstruction.

From the beginning of x-ray CT, the effects of beam hardening have been an issue in achieving high-quality images. In absorption CT, beam-hardening artifacts are the result of the energy spectrum dependence of the linear attenuation coefficient. In DPC-CT, the refractive index decrement δ is still dependent on the energy spectrum. Meanwhile, polyenergetic beams are attenuated more at lower energies, which will change the energy spectrum of these beams (Chabior *et al* 2011). Thus, due to the absorption of the sample, beam-hardening artifacts will make their way into DPC-CT images. The beam-hardening artifacts and their correction will also be studied in the future.

Acknowledgments

This work was supported by the National Natural Science Foundation of China (grant no. 61071210). The authors would like to thank Hengyong Yu for his valuable help.

References

- Bevins N, Zambelli J, Li K, Qi Z and Chen G-H 2012 Multicontrast x-ray computed tomography imaging using Talbot–Lau interferometry without phase stepping *Med. Phys.* **39** 424–8
- Bravin A, Coan P and Suortti P 2013 X-ray phase-contrast imaging: from pre-clinical applications towards clinics *Phys. Med. Biol.* **58** R1–R35
- Chabior M, Donath T and David C 2011 Beam hardening effects in grating-based x-ray phase-contrast imaging *Med. Phys.* **38** 1189–95
- Chen G and Qi Z 2008 Image reconstruction for fan-beam differential phase contrast computed tomography *Phys. Med. Biol.* **53** 1015–25
- Chong W, Yang J and Wang G 2012 Differential phase-contrast interior tomography *Phys. Med. Biol.* **57** 2905–14
- Diemoz P C, Coan P, Glaser C and Bravin A 2010 Absorption, refraction and scattering in analyzer-based imaging: comparison of different algorithms *Opt. Express* **18** 3494–509
- Fu J, Li P, Wang Q L, Wang S Y, Bech M, Tapfer A and Pfeiffer F 2011 A reconstruction method for equidistant fan beam differential phase contrast computed tomography *Phys. Med. Biol.* **56** 4529–38
- Fu J, Velroyen A, Tan R, Zhang J, Chen L, Tapfer A, Bech M and Pfeiffer F 2012 A reconstruction method for cone-beam differential x-ray phase-contrast computed tomography *Opt. Express* **20** 21512–9
- Huang Z F, Kang K J, Zhang L, Chen Z Q, Ding F, Wang Z T and Fang Q G 2009 Alternative method for differential phase-contrast imaging with weakly coherent hard x rays *Phys. Rev A* **79** 013815
- Itoh H, Nagai K and Sato G 2011 Two-dimensional grating-based x-ray phase-contrast imaging using Fourier transform phase retrieval *Opt. Express* **35** 3339–46
- Katsevich A 2002 Theoretically exact filtered-backprojection type inversion algorithm for spiral CT *SIAM J. Appl. Math.* **62** 2012–26
- Katsevich A 2004 An improved exact filtered backprojection algorithm for spiral computed tomography *Adv. Appl. Math.* **32** 681–97
- Kottler C, David C, Pfeiffer F and Bunk O 2007 A two-directional approach for grating based differential phase contrast imaging using hard x-rays *Opt. Express* **15** 1175–81
- Lauzier P T, Qi Z and Zambelli J 2012 Interior tomography in x-ray differential phase contrast CT imaging *Phys. Med. Biol.* **57** N117–30
- Li J, Zhu P and Sun Y 2012 An approximate reconstruction method for helical cone-beam differential phase-contrast computed tomography images *Phys. Med. Biol.* **57** 2347–57
- Munro P R, Ignatyev K, Speller R D and Olivo A 2010 The relationship between wave and geometrical optics models of coded aperture type x-ray phase contrast imaging systems *Opt. Express* **18** 4103–17
- Munro P R, Ignatyev K, Speller R D and Olivo A 2012 Phase and absorption retrieval using incoherent x-ray sources *Proc. Natl Acad. Sci. USA* **109** 13922–7

- Nilchian M, Vonesch C, Modregger P, Stampanoni M and Unser M 2013 Fast iterative reconstruction of differential phase contrast x-ray tomograms *Opt. Express* **21** 5511–28
- Noo F, Pack J and Heuscher D 2003 Exact helical reconstruction using native cone-beam geometries *Phys. Med. Biol.* **48** 3787–818
- Olivo A, Ignatyev K, Munro P R and Speller R D 2011 Noninterferometric phase-contrast images obtained with incoherent x-ray sources *Appl. Opt.* **50** 915–7
- Pfeiffer F, Weitkamp T, Bunk O and David C 2006 Phase retrieval and differential phase-contrast imaging with low-brilliance x-ray sources *Nature Phys.* **2** 258–61
- Qi Z, Thériault-Lauzier P, Bevins N, Zambelli J, Li K and Chen G 2011 Helical x-ray differential phase contrast computed tomography *Proc. SPIE* **7961** 79611Q
- Revol V, Kottler C, Kaufmann R, Jerjen I, Luthi T, Cardot F, Niedermann P, Straumann U, Sennhauser U and Urban C 2010 X-ray interferometer with bent gratings: towards larger fields of view *Nucl. Instrum. Methods Phys. Res. A* **648** S302–5
- Sato G, Itoh H and Kondoh T 2011 Two-dimensional gratings-based phase-contrast imaging using a conventional x-ray tube *Opt. Lett.* **36** 3551–3
- Suetens P 2009 *Fundamentals of Medical Imaging* (Cambridge: Cambridge University Press)
- Tan J, Li H, Parikh P, Izaguirre E and Yang D 2012 Implementation and evaluation of helical on-board CBCT and exact image reconstruction *Med. Phys.* **39** 3973–83
- Tuy H 1983 An inversion formula for cone-beam reconstruction *SIAM J. Appl. Math.* **43** 546–52
- Vedantham S and Karellas A 2013 X-ray phase contrast imaging of the breast: analysis of tissue simulating materials *Med. Phys.* **40** 041906
- Wen H, Bennett E, Kopace R, Stein A F and Pai V 2010 Single-shot x-ray differential phase contrast and diffraction imaging using two-dimensional transmission gratings *Opt. Lett.* **35** 1932–4
- Wu Z, Gao K, Wang Z L, Ge X, Chen J, Wang D J, Pan Z Y, Zhang K, Zhu P P and Wu Z Y 2013 A new method to retrieve phase information for equiangular fan beam differential phase contrast computed tomography *Med. Phys.* **40** 031911
- Xu Q F, Sidky E Y, Pan X C, Stampanoni M, Modregger P and Anastasio M A 2012 Investigation of discrete imaging models and iterative image reconstruction in differential x-ray phase-contrast tomography *Opt. Express* **20** 10724–49
- Yu H and Wang G 2004 Studies on implementation of the Katsevich algorithm for spiral cone-beam CT *J. X-Ray Sci. Technol.* **12** 97–116
- Zanette I, Bech M, Pfeiffer F and Weitkamp T 2011 Interlaced phase stepping in phase-contrast x-ray tomography *Appl. Phys. Lett.* **98** 094101
- Zhu P, Zhang K and Wang Z 2010 Low-dose, simple, and fast grating-based x-ray phase-contrast imaging *Proc. Natl Acad. Sci. USA* **107** 13576–81
- Zou Y and Pan X 2004 Exact image reconstruction on PI-lines from minimum data in helical cone-beam CT *Phys. Med. Biol.* **49** 941–59